

Micro-wrinkling and delamination-induced buckling of stretchable electronic structures

O. K. Oyewole, D. Yu, J. Du, J. Asare, D. O. Oyewole, V. C. Anye, A. Fashina, M. G. Zebaze Kana, and W. O. Soboyejo

Citation: [Journal of Applied Physics](#) **117**, 235501 (2015); doi: 10.1063/1.4922665

View online: <http://dx.doi.org/10.1063/1.4922665>

View Table of Contents: <http://scitation.aip.org/content/aip/journal/jap/117/23?ver=pdfcov>

Published by the [AIP Publishing](#)

Articles you may be interested in

[Buckling-driven delamination of carbon nanotube forests](#)

Appl. Phys. Lett. **102**, 223103 (2013); 10.1063/1.4802080

[Buckling induced delamination of graphene composites through hybrid molecular modeling](#)

Appl. Phys. Lett. **102**, 031902 (2013); 10.1063/1.4788734

[Localized exfoliation versus delamination in H and He coimplanted \(001\) Si](#)

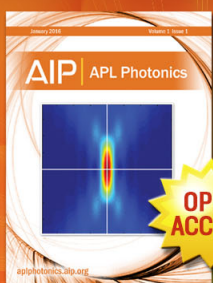
J. Appl. Phys. **105**, 093528 (2009); 10.1063/1.3116738

[Electromigration-induced extrusion failures in Cu/low- \$k\$ interconnects](#)

J. Appl. Phys. **104**, 023529 (2008); 10.1063/1.2957057

[Nano- and microscale adhesion energy measurement for Au–Au contacts in microswitch structures](#)

J. Appl. Phys. **100**, 104313 (2006); 10.1063/1.2388688



Launching in 2016!
The future of applied photonics research is here

AIP | APL
Photonics

Micro-wrinkling and delamination-induced buckling of stretchable electronic structures

O. K. Oyewole,^{1,2} D. Yu,^{3,4} J. Du,^{3,4,5} J. Asare,¹ D. O. Oyewole,^{6,7} V. C. Anye,⁶ A. Fashina,¹ M. G. Zebaze Kana,^{2,7} and W. O. Soboyejo^{3,4,6,a)}

¹*Department of Theoretical and Applied Physics, African University of Science and Technology, Km 10, Airport Road, Galadimawa, Abuja, Federal Capital Territory, Nigeria*

²*Department of Materials Science and Engineering, Kwara State University, Malete, P.M.B 1530, Ilorin, Kwara State, Nigeria*

³*Department of Mechanical and Aerospace Engineering, Princeton University, Olden Street, Princeton, New Jersey 08544, USA*

⁴*Princeton Institute of Science and Technology of Materials, Princeton University, 70 Prospect Street, Princeton, New Jersey 08544, USA*

⁵*Department of Mechanical and Nuclear Engineering, The Pennsylvania State University, 137 Reber Building, University Park, Pennsylvania, USA*

⁶*Department of Materials Science and Engineering, African University of Science and Technology, Km 10, Airport Road, Galadimawa, Abuja, Federal Capital Territory, Nigeria*

⁷*Physics Advanced Laboratory, Sheda Science and Technology Complex, P.M.B 186, Garki, Abuja, Federal Capital Territory, Nigeria*

(Received 22 February 2015; accepted 4 June 2015; published online 17 June 2015)

This paper presents the results of experimental and theoretical/computational micro-wrinkles and buckling on the surfaces of stretchable poly-dimethylsiloxane (PDMS) coated with nano-scale Gold (Au) layers. The wrinkles and buckles are formed by the unloading of pre-stretched PDMS/Au structure after the evaporation of nano-scale Au layers. They are then characterized using atomic force microscopy and scanning electron microscopy. The critical stresses required for wrinkling and buckling are analyzed using analytical models. The possible interfacial cracking that can occur along with film buckling is also studied using finite element simulations of the interfacial crack growth. The implications of the results are discussed for potential applications of micro-wrinkles and micro-buckles in stretchable electronic structures and biomedical devices. © 2015 AIP Publishing LLC. [<http://dx.doi.org/10.1063/1.4922665>]

I. INTRODUCTION

Stretchable electronics have emerged as interesting technologies for several applications in which stretchability is considered important.^{1–15} These applications include stretchable electrical inter-connects,^{1–5} optical sensors and diffraction gratings,^{6,7} metrology for the measurement of elastic moduli,^{8,9} templates for device fabrication,¹⁰ stretchable electronics,^{1,3,11,12} micro-contact printing stamps,^{13,14} cell culture substrates,¹⁵ and surfaces for cell contact guidance¹⁶ in implantable biomedical devices.

However, mechanical flexibility is a pre-requisite to achieve organic¹² and inorganic^{2–5,17} stretchable electronics, where wrinkling and buckling deformations are used to create wavy, out of plane structures, which can accommodate strain. This is done by pre-stretching the substrates^{3,5,9} before the deposition of the devices. The wrinkled and delamination-induced buckled structures of the devices are formed due to thermal compressive residual^{11,18–20} and pre-stretch^{3,5,9} stresses. The formation and deformation of wrinkling of thin films can initiate failure, which can lead to delamination²¹ in layered structures of stretchable electronics.

Prior work by Rogers and co-workers^{3,4,17,22} has identified the importance of buckling as a strategy for achieving

stretchable electronics, stretchable optoelectronic devices, stretchable integrated systems, stretchable metallic interconnect, and emerging stretchable curvilinear systems for biomedical applications. The formation of wrinkles of thin film-coated polymeric structures has also been observed by Watanabe²⁰ for checkerboard patterning.

In the case of wrinkling, layered devices adhere to substrate, upon release of pre-strain. During service conditions, by stretching the wrinkled structure below the critical pre-strain levels, the wavy structures will become plane, while the interfacial contact remains intact. However, the nucleation and growth of cracks along the interfaces can cause interfacial failure to occur under static or cyclic loading conditions above threshold conditions. This can lead ultimately to adhesive or cohesive failure. Mei and Huang¹⁹ and Ebata *et al.*²¹ have shown that the wrinkled surfaces are formed due to compression-induced buckling instability of thin films, which can lead to interfacial cohesive failure and delamination.

On the other hand, a buckled morphology of the layered structure can occur in the presence of interfacial voids, before and after the release of the pre-stretch. This failure mode can also occur due to merging of the possible micro voids that can lead to delamination.^{19,21} Interfacial cracks are also formed from sandwiched dust particles²³ and bubbles²⁴ between the deposited films and substrates. Residual stress can also drive the delamination of the layered

^{a)}Author to whom correspondence should be addressed. Electronic mail: soboyejo@aol.com

structures from substrate. The interfacial cracks then grow under static or cyclic loading conditions until critical conditions are reached. It is, therefore, important to study the possible interfacial adhesion and contact of micro-wrinkled and buckled structures.

In an effort to further understand the mechanics of thin films on elastomeric substrates, Hutchinson and Suo²⁵ have shown that when compressive stresses in the films exceed the critical buckling stress, the film can buckle away from the substrate, for a given interfacial crack length. Angstrom-scale periodic buckling patterns have been observed in free-standing graphene bilayers generated by liquid-phase processing,²⁶ while non-sinusoidal surface profiles of buckled gold thin films have been observed on elastomeric substrates.²⁷ Furthermore, finite width effects have been elucidated using experiments and models,²⁸ while the deformation of a stretchable single crystal silicon has been studied on elastomeric substrates.²⁹

Theoretical and numerical schemes have been used by Domokos *et al.*³⁰ to study the elastic buckling of an inextensible beam with fixed end displacements, restricted to the plane, and in the presence of rigid, frictionless side-walls. Holmes *et al.*³¹ have also studied the buckling of an inextensible rod, restricted to the plane, with free ends, and in the presence of distributed body forces derived from a potential. The effects of plasticity on buckling patterns in thin films on elastomeric substrates have also been studied using finite element simulation to reveal different patterns of buckling.³²

The delamination-induced buckling of semiconductor nano-ribbons (on the surfaces of elastomers) can be precisely controlled²² with periodic, inactivated, and activated regions. Ordered buckled structures can also occur on thin metal films, due to the thermal contraction of elastomeric polymer substrates.³³ Furthermore, the controlled formation of ordered, sinusoidal wrinkles has also been associated with the effects of plasma oxidation of a compliant polymer.³⁴ Periodic sinusoidal structures have also been developed for buckled ribbons of piezoelectric ceramic (PZT)³⁵ and tunable diffraction gratings.¹⁰

In an effort to develop robust systems for stretchable electronics, the level of strain-to-wrinkling had been modeled in literature. A well-known analytical solution^{22,28} has been used to predict critical strain for the onset of wrinkling of thin films on pre-strained polymeric substrates with small and large pre-strains.^{5,19,20,22,28} Jiang *et al.*²⁸ have obtained the analytical solution for the buckling geometry and maximum strain in buckled thin film using nonlinear buckling model. Sun *et al.*²² have also analyzed the incompressible substrate deformation of a folding wrinkled structures using neo-Hookean non-linear elasticity, while Huang *et al.*³⁶ have presented nonlinear analyses of wrinkle formation in films bonded to compliant substrates. The wrinkling was due to compressive stresses,³⁷ which buckled the films on the polymeric substrates after deposition.

Significant efforts have been reported on nanotubes on stretchable substrates. Harris *et al.*³⁸ have reported the electronic and optical properties of thin films of single-walled carbon nanotubes on polymeric substrates. They had studied the underlying failure mechanisms, for significant differences

in the electronic manifestations of the thin films using wrinkling. Hobbie *et al.*³⁹ have also reported that the dominant wavelength of the wrinkled structures of single-wall carbon nanotubes deposited on pre-strain poly(dimethylsiloxane) (PDMS) decreases with pre-strain, while Wang *et al.*⁴⁰ have shown that the amplitude and periodicity of buckled graphene films on flexible substrates reduce with the increasing in pre-strain.

In the case of self-assembled materials, Ramanathan *et al.*⁴¹ have described the role of confinements on wrinkling structures using compressive strains. Wang *et al.*⁴² have presented the experimental investigation of fracture in self-assembled gold nanoparticle layers on polymeric substrates. They showed that the fracture strength of the gold nanoparticles increases as the size of the particles increases, but decreases as the layer thickness increases.

In case of thin films of gold deposited on pre-strained PDMS substrates, Fei *et al.*²⁷ have analyzed the profile of gold-PDMS structure using experiments and finite element models. They showed that the profile of the structure depends on film thickness, the level of pre-strain and the rate at which the strain is being released. Therefore, the different profiles of thin-film coated PDMS substrates can be attributed to the effects of strain localization, when the pre-strain exceeds the critical strain. Ebata *et al.*²¹ have also shown that the amplitude of the wrinkled, folded, and delaminated profile of such structures depends on the applied strain.

However, there are no prior studies that use the occurrence of wrinkling and delamination-induced buckling in the combined measurement of film elastic properties and interfacial fracture toughness between thin metal films and elastomeric substrates. This is done in this paper using the results of a combined analytical, computational, and experimental study of micro-wrinkling and interfacial fracture of the delamination-induced buckling of nano-scale Au films on elastomeric poly-dimethylsiloxane (PDMS) substrates that are relevant to stretchable electronics and implantable stretchable biomedical devices. Analytical models are used to determine the critical stresses required for wrinkling and delamination-induced buckling in the structures. Interfacial fracture mechanics concepts are also used to determine the interfacial fracture toughness between the Au films and the PDMS substrates. The implications of the results are then discussed for the design of stretchable electronics and biomedical devices.

The paper is divided into five sections. Following the introduction in Sec. I, the models are presented in Sec. II before describing the experimental and computational methods in Sec. III. The results and discussion are then presented in Sec. IV, before summarizing the salient conclusions from this work in Sec. V.

II. THEORY

This section presents the models that were used in this work. They include (i) the theory of interfacial adhesion between two dissimilar materials; (ii) analytical models of the wrinkling and buckling of thin films on stretchable

substrates; and (iii) interfacial fracture mechanics models of crack growth between layers.

A. Adhesion

1. Adhesion force

The adhesion force between two materials can be measured using contact mode atomic force microscopy (AFM).⁴³ This method has been used in the literature^{44,45} for the measurement of adhesion in flexible/stretchable inorganic, organic, and hybrid organic-inorganic electronic structures. First, the AFM tip is coated with one material, while the substrate is coated with the second material. The steps involved in the measurement of the adhesion force are illustrated in Figure 1. These were used to measure the force-displacement behavior due to adhesive interactions and the elastic deformation of the AFM tips.

The cantilever tip begins at point A, at a distance from the substrate. In this case, there is minimal long-range attractive force, so there is no deflection of the tip on the force-displacement between A and B (Figure 1). However, as the tip is lowered towards the surface, it jumps into contact. This is due to increasing adhesive attractive forces, as the tip approaches point B. Subsequently, the tip bends under elastic deformation, as the deflection increases past point C. The process is then reversed after loading the tip to a maximum force. However, as the tip is reversed, it does not detach at zero force. This is due to the effects of adhesion at point D. Instead, the reversed loading must be continued to point E, at which the force is sufficient to overcome the adhesive interactions. The adhesion force, F , can thus be calculated from Hooke's law. This gives

$$F = -kx, \quad (1)$$

where x is the tip displacement (A-E) and k is the spring constant of the AFM tip. The spring constant, k , of each AFM tip was measured using the thermal tune method.⁴⁶

2. Adhesion energy

There are several possible models that can be used to estimate the adhesion energy. These include the Derjaguin–Muller–Toporov (DMT) model,⁴⁷ the

Johnson–Kendall–Robert (JKR) model,⁴⁸ and the Maugis–Dugdale (MD) model.⁴⁹ A dimensionless parameter is determined to distinguish the use of these models.^{44,46–49} If the parameter is less than 0.1, the DMT model is applied. If it is greater than 5.0, the JKR is applied. The intermediate values of the dimensionless parameter correspond to MD model. In the case of weak interactions between stiff materials with small radii, the DMT model is applied.

Rahbar *et al.*⁵⁰ have used DMT model to similar cases like this, while a general framework for extracting adhesion energies from AFM indentation experiments in multilayered drug-eluting stents has been presented.^{51,52} Akogwu *et al.*⁴⁴ have also studied adhesion of stretchable gold coated PDMS using DMT model. The adhesion energy, γ , is related to the adhesion force, $F_{adhesion}$, by the following expression:

$$\gamma = F_{adhesion}/2\pi R, \quad (2)$$

where R is the effective radius, which is given by

$$1/R = (1/R_{tip}) + (1/R_{rms}), \quad (3)$$

where R_{rms} is the root-mean-squared roughness of the substrate and R_{tip} is the radius of the coated AFM tip.

B. Residual and applied stresses

The controlled formation of wrinkles and buckles for applications in stretchable electronics involves the deposition of thin films onto pre-stretched substrates.^{1–5,12} The film is subjected to stresses due to two factors. One is from the thermal expansion mismatch between the film and the substrate, while the other is from the pre-stretch of the substrate. These stresses are responsible for the induced wrinkling and buckling. The residual stress, σ_{th} , due to the thermal expansion coefficient mismatch is given by⁴⁴

$$\sigma_{th} = [E_f(\alpha_f - \alpha_s)(T_d - T)]/(1 - \nu_f), \quad (4)$$

where E_f and ν_f are Young's modulus and Poisson's ratio of the film; α_f and α_s are the respective thermal expansion coefficients of the film and the substrate; T_d is the deposition temperature, and T corresponds to the room temperature. The stress, σ_{app} , due to the release of the applied pre-stretched substrate can be approximated as

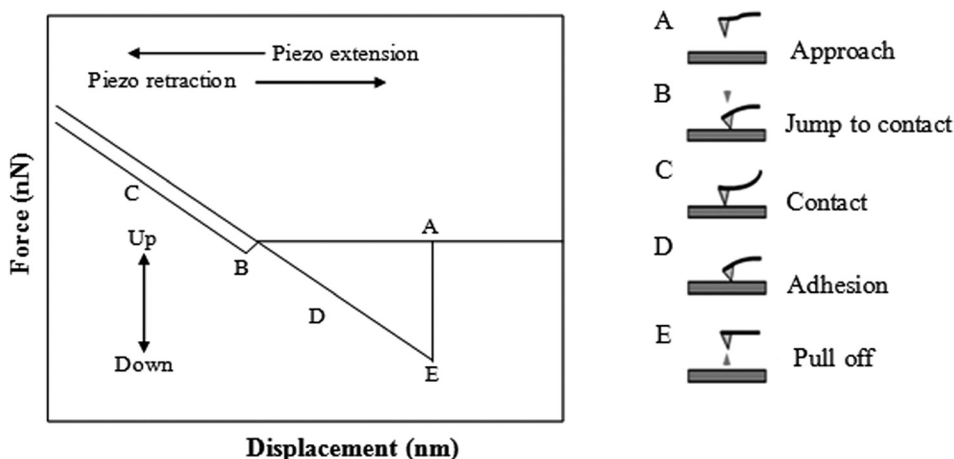


FIG. 1. Schematic of force-displacement curve for various stages from A to E. (Ref. 54).

$$\sigma_{app} = E_f \varepsilon_{pre}, \quad (5)$$

where ε_{pre} corresponds to the pre-strain. By applying the principle of linear superposition, the total stress in the film can be obtained from the summation of Eqs. (4) and (5). This is given by

$$\sigma_R = \sigma_{th} + \sigma_{app} = [E_f(\alpha_f - \alpha_s)(T_d - T)]/(1 - \nu_f) + E_f \varepsilon_{pre}. \quad (6)$$

Equation (6) is the total stress that is responsible for wrinkling and delamination-induced buckling in the thin film deposited on a pre-stretched polymeric substrate.

C. Wrinkling and buckling models for stretchable electronics

As described above in Sec. II B, wrinkled and buckled structures are formed as a result of the total stress on the film. The film starts wrinkling or buckling when the induced stress reaches a critical value. The solutions of the critical stress, σ_c , for the onset of wrinkling or buckling of thin films are given by^{5,19,20}

$$\sigma_c = [E_f/(1 - \nu_f^2)]^{1/3} [3E_s/8(1 - \nu_s^2)]^{2/3}, \quad (7)$$

where E_f and E_s are the Young's moduli of the film and the substrate, ν_f and ν_s are the Poisson's ratios of the film and the substrate. Also, the buckling of thin metallic films on stretchable elastic substrates has been modeled by Hutchinson and Suo.²⁵ The critical stress can be expressed as a function of wavelength of the buckling.^{25,44} This is given by

$$\sigma_c = \pi^2 h^2 E_f / 3 \lambda^2 (1 - \nu_f^2), \quad (8)$$

where λ is the wavelength of the buckle, E_f is the film Young's modulus, ν_f is the film Poisson's ratio, and h is the film thickness.

D. Interfacial fracture mechanics

In this section, interfacial failure is modeled at the onset of buckling of thin films on PDMS substrates. The theoretical expressions are presented for the energy release rates and the adhesion energies. It is assumed that films that are deposited on pre-stretched substrates can delaminate due to buckling,²⁵ sandwiched particles and voids.²⁴

1. Analytical modeling

The buckling of thin metallic films is often accompanied by the delamination of the films from the substrates. The buckled profiles can be analyzed using interfacial fracture mechanics. The energy release rate, G , of the interfacial crack is given by²⁵

$$G = [(1 - \nu_f^2)h/(2E_f)](\sigma_R - \sigma_c)(\sigma_R + 3\sigma_c), \quad (9)$$

where E_f and ν_f are the Young's modulus and the Poisson's ratio of the Au film, h is the thickness of Au film, σ_R is the residual stress in the film, and σ_c is the critical buckling

stress. Ebata *et al.*²¹ have shown that the residual stress increases with increasing amplitude of the buckling, as delamination proceeds. The thin film starts to delaminate from the substrate when the total stress (σ_R) is more than the critical stress (σ_c) for buckling. Hence, the interfacial energy release rate, G , increases with increasing σ_R and approaches its critical value, G_c , which is given by

$$G_c = [(1 - \nu_f^2)h/2E_f]\sigma_R^2. \quad (10)$$

However, the interfacial adhesion between two dissimilar materials involves interactions between atoms on the two surfaces to form secondary bonds. The true work of adhesion between the film and the substrate materials is given by^{44,53,54}

$$G_{adhesion} = G_{elastic} = \gamma_f + \gamma_s - \gamma_{f-s}, \quad (11)$$

where γ_f and γ_s are the surface energies of the film and substrate separately, while γ_{f-s} is the surface energy between the film and the substrate in contact. If the bonds were broken mechanically, high interfacial fracture energies can be obtained due to the contributions from plastic deformation. However, if the contributions from plasticity are small, then the adhesion energy can be approximated as the interfacial fracture energy⁵³ between the two different materials.

From a fracture mechanics perspective, the measured adhesion energy, γ , corresponds to the critical mode I energy release rate.⁵⁴ This is possible because the fracture mechanics approach uses the applied strain energy release rate to measure the practical work of adhesion.⁵³ Hence, $G_c \approx \gamma$. The critical interfacial energy release rates can also be computed using commercial software packages, such as ABAQUSTM, which was used in this study (ABAQUS 6.12, Dassault Systèmes Incorporation, Rhoda Island). This involves introducing the geometry, materials properties, and the boundary conditions of the bi-layered system into the software. In this case, the rate of the energy released at the tip of the onset interfacial crack is denoted by G_{comp} .

III. MATERIALS AND METHODS

A. Experimental methods

1. Formation of wrinkled and micro-buckled Au on PDMS substrates

First, the PDMS substrate was prepared by mixing a Slygard 184 silicone elastomer curing agent with a Slygard 184 silicone elastomer base (Dow Corning Corporation, Midland MI) in a 1:10 weight ratio. Then, the mixture was processed under a vacuum pressure of 6 kPa for 30 min to remove all possible bubbles. The processed PDMS was poured into an aluminum mold with a dog-bone shape. This was followed by annealing in an oven at 80 °C for 2 h to form a 1 mm thick PDMS substrate.

The PDMS was fixed with clamps at both ends and pre-strained to different levels (18%, 36%, and 70%) on a hard steel substrate. A 5 nm thick of chromium (Cr) adhesive layer was then deposited onto the PDMS substrate using Denton evaporator (Denton DV 502 A, Denton Vacuum,

Moorestown, NJ). Chromium layer was used to improve the interfacial adhesion between the Au-film and the substrate. A gold thin film layer with a thickness of 100 nm was then deposited on top of the chromium layer. After deposition, the two ends of the PDMS substrate were released, and the wrinkle/buckle patterns were formed spontaneously in the gold thin films.

2. AFM adhesion measurements

The interfacial adhesion in the layered Au-Cr-PDMS structure was measured using AFM. First, etched silicon contact mode AFM tips were purchased from Veeco Instruments Woodbury, NY. The AFM tips were then coated with Au and Cr separately, while Au was deposited on glass substrates using Denton evaporator (Denton DV 502 A, Denton Vacuum, Moorestown, NJ). With these coated tips and substrates, the adhesion forces between Cr/PDMS (Cr-coated tip versus PDMS), Cr/Au (Cr-coated tip versus Au-coated glass), and Au/PDMS (Au-coated tip versus PDMS) interfaces were measured.

AFM measurements were performed in air over a temperature range of 22–25 °C and a relative humidity range of 31–46%. The tests were carried out in a Bruker Instruments Dimension 3000 AFM (Bruker Instruments, Plainview, NY). About ten force-displacement curves were obtained for each interaction. The tip deflections were obtained from the curves. The spring constants of each of the tips were measured using the thermal tune method.⁴⁶ This was done using a Bruker Instruments Nanoscope IIIa AFM (Bruker Instruments, Plainview, NY). With the measurements of the tip deflections and the spring constants, the adhesion forces were finally obtained from Hooke's law (Eq. (1)).

Due to the high sensitivity of AFM measurements to surface roughness, the substrate roughnesses and the tip radii were measured for each interaction pair. The surface roughnesses were obtained by AFM in the tapping mode. About 10 height and phase images of each substrate were obtained. These were used to measure the root mean squared roughnesses. The tip radii were calculated (before and after measurement) from images obtained using a scanning electron microscope (SEM,

Philips FEI XL30 FEG-SEM, Hillsboro, OR). The measurements of the surface roughness and the tip radii were used to calculate the adhesion energies from Eqs. (2) and (3).

B. Computational methods

Computational methods were used to study the failure mechanisms in the thin films of Au on PDMS substrates due to wrinkling and buckling. These were used to provide insights into the experimental results. First, the stress distributions in the wrinkled Au-films were simulated using the ABAQUSTM software package (ABAQUS 6.12, Dassault Systèmes Incorporation, Rhoda Island). The two ends of the Au-PDMS model were displaced (pre-strained) by 18%, 36%, and 70% of the length of the structure. The modulus and Poisson ratio of the Au films were maintained at 61 GPa and 0.35,⁵⁵ respectively. However, the Young's modulus of the PDMS substrate depends on the fabrication curing conditions and the mixing ratio of base and curing agent of the Slygard silicone elastomer.⁵⁶ Hence, in the finite element simulation, the modulus of the substrate was varied from 1 MPa to 100 MPa, with Poisson ratio of 0.3.⁵⁵ This was done to provide insights into the effects of substrate Young's modulus on the wrinkling profile.

In the case of delamination-induced buckling, it was assumed that there were pre-existing interfacial cracks between the Au-film and PDMS substrates. These cracks can be attributed to imperfections, such as voids, bubbles, or impurities that are present at the interfaces. The energy release rates at the tips of the cracks were computed in form of the path independent J-integral. These were determined as functions of crack length using the ABAQUSTM software package for the three levels of pre-strains. Furthermore, for different interfacial crack lengths, the interfacial energy release rates were calculated as functions of the pre-strain.

Since the film thickness is very small compared to the thickness of the substrate, and the fact that the Young's modulus of the film is far greater than that of the substrate, fine mesh was used to model the Au/PDMS interface (as shown in Figure 2). Four-node plane strain quadrilateral elements were used. All the materials properties that were used were

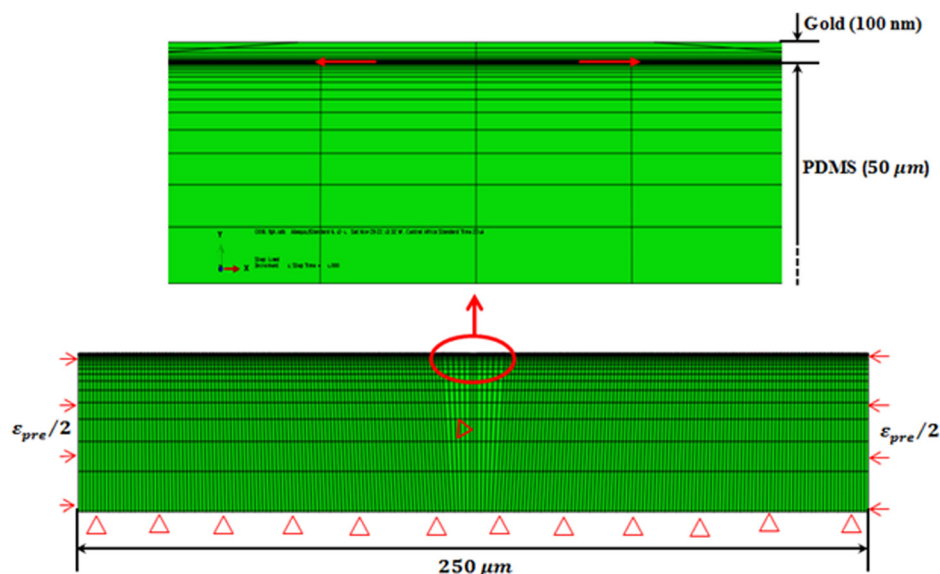


FIG. 2. Finite element model of buckling of thin gold film on PDMS substrate.

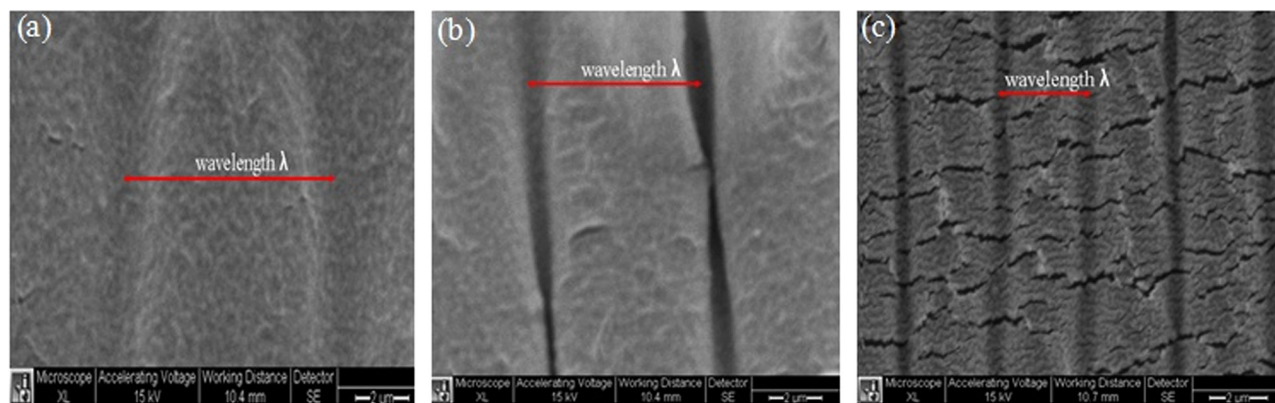


FIG. 3. Micro-wrinkle profiles for different pre-strain values of (a) 18%, (b) 36%, and (c) 70%.

assumed to exhibit isotropic behavior, while the active contact Au/PDMS interface was maintained at zero rotation.

IV. RESULTS AND DISCUSSION

A. Wrinkling profile as a function of pre-strain and substrate elastic modulus

SEM images of the wrinkled profiles induced after the release of the pre-strained Au/PDMS samples are presented in Figures 3(a)–3(c). The images show that the wavelengths of the wrinkled structure reduced from 9.7 μm, for a pre-strain of 18%, to 6.6 μm, for a pre-strain of 36%, and 3.0 μm, for a pre-strain of 70%. This is presented clearly in Figure 4. The wavelengths are, therefore, inversely related to the pre-strain values. Furthermore, some transverse cracking was observed in the Au films, especially after pre-straining to a level of 70% (Figure 3(c)). The reduction in the wavelengths is attributed to the effects of the propagating transverse cracks, due to increasing pre-strain.

The von Mises stress distributions in the Au/PDMS structure are presented in Figures 5(a)–5(d). These show the dependence of substrate elastic modulus on stress distributions and profile amplitude. The increase in the elastic modulus of the substrate increases the concentration of stress in the wrinkled structure. Hence, the processing of stiffer PDMS substrates will increase the overall Mises stresses, as shown in Figures 5(a)–5(d). Furthermore, the wrinkling

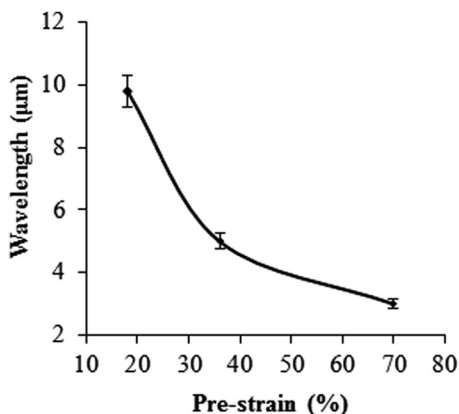


FIG. 4. The wavelength of the profile versus pre-strain value of the PDMS substrate.

profile became more well defined with increasing substrate Young’s modulus (Figures 5(a)–5(d)). However, there is a high possibility that failure would be induced by the higher Von Mises stresses in the Au/PDMS structures that have higher moduli. A balanced approach is, therefore, needed to obtain well defined wrinkled profiles without inducing failure.

B. Stress analysis

1. Residual stress

For the Au film deposited on a pre-stretched PDMS substrate, residual stresses were induced in the Au films due to the thermal expansion coefficient mismatch between the Au films and the PDMS substrate. The total stress in the Au films was also assumed to be the sum of the thermal mismatch stress and the stress due to pre-strained PDMS

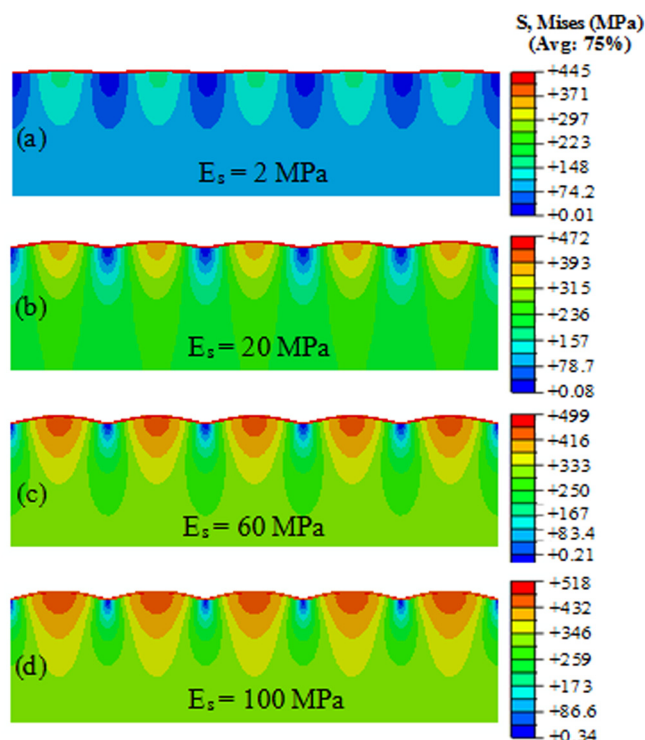


FIG. 5. Von Mises showing the dependence of elastic modulus of the substrate on wrinkle profile of Au film on PDMS substrate at 36% pre-strain.

TABLE I. Residual stresses due to effects of thermal expansion coefficient mismatch and pre-strained PDMS substrate.

Pre-strain (%)	Applied stress σ_{app} (GPa)	Residual stress σ_R (GPa)
18	10.98	11.56
36	21.96	22.54
70	42.70	43.28

substrate. The average textured Young's modulus for the Au film has been obtained to be ~ 61 GPa (Ref. 55). The measured Young's modulus of the Au film was then incorporated into Eq. (4), along with the temperature difference ($\Delta T = T_d - T = 292$ K), the Poisson ratio ($\nu_f = 0.35$), and thermal expansion coefficients of the Au-film ($\alpha_f = 1.4 \times 10^{-5}/\text{K}$) and substrate ($\alpha_s = 3.14 \times 10^{-4}/\text{K}$). These were used to estimate the residual stress due to thermal expansion mismatch to be ~ 0.583 GPa. The stress due to the pre-strained PDMS substrate (Table I) was calculated using Eq. (5). Hence, the sum of the two residual stresses (σ_R) was obtained using Eq. (6) for different thicknesses of the Au film. These results are presented in Table I. These show that the calculated total stress increase with increasing pre-strain of the PDMS substrate.

2. Critical stresses

The calculated critical stresses obtained for different wavelengths are presented in Figure 6(a). The critical

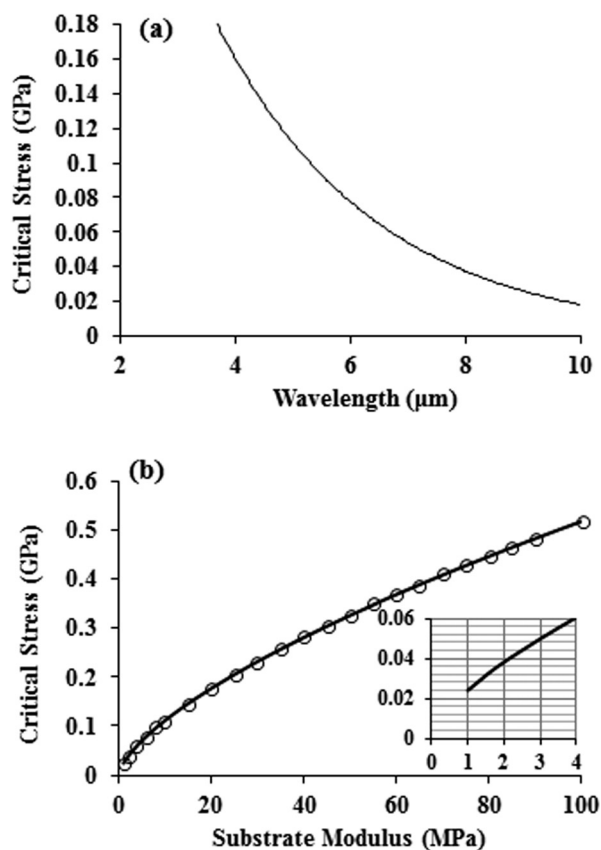


FIG. 6. Dependence of (a) profile wavelength on critical stress and (b) substrate modulus on critical stress.

TABLE II. Average surface roughness values.

Surface	Roughness (nm)
PDMS on glass	0.7 ± 0.1
Cr	9.9 ± 2.2
Au	3.4 ± 0.5

stresses for the onset of wrinkling/buckling were estimated from the measured profiles (Figure 3 and Eq. (8)). The critical stress decreases with increasing wavelength and vice-versa. Therefore, the critical stress is inversely related to the wavelength of the buckling/wrinkling profile. The decrease in the critical stress is attributed to the increase in pre-strain, which increases transverse cracks observed in Figure 3. It is important to note that the transverse cracks can be attributed to the possible formation of a brittle silica-like layer in the near-surface region of the PDMS with the deposited Cr. However, in Figure 6(b), the critical stress increases with increasing substrate Young's modulus. Figure 6(b) was obtained from Eq. (7), for possible ranges (1–100 MPa) of PDMS Young's moduli. The limiting critical stress for the Au thin film on a specific stretchable substrate (of known modulus) can be predicted from Figure 6(b). For example, in Figure 6(b) inset, the critical stresses of Au film on PDMS substrates with Young's moduli of 1 MPa and 4 MPa are approximately 0.024 GPa and 0.06 GPa, respectively.

C. Surface roughness/profile

The root-mean-squared (rms) roughnesses of the different layers in the Au-coated PDMS structures are presented in Table II. The PDMS had an rms roughness of 0.7 ± 0.1 nm, while the Cr-coated surface had an rms roughness of 9.9 ± 2.2 nm. The Au film has an intermediate rms roughness of 3.4 ± 0.5 nm. The AFM tip radii measured from the SEM tip images averaged ~ 250 nm (Figure 7). Both the surface roughnesses and the AFM tips radii were used for computation of adhesion energies. In the SEM images, there were no significant changes observed in the AFM tips. The highest magnification SEM images did not reveal any evidence of

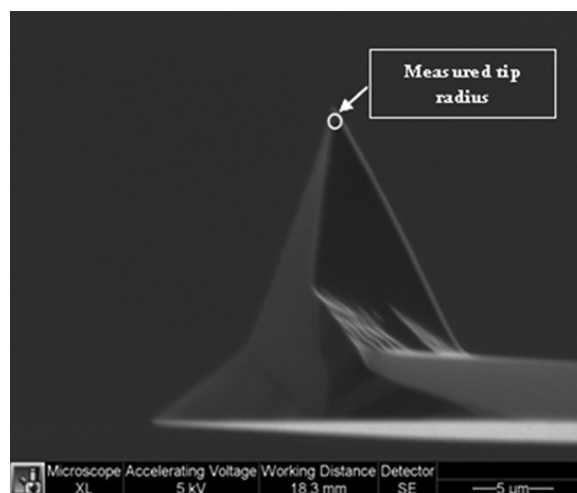


FIG. 7. SEM image of AFM tip profile.

cohesive failure in the adhesion force measurement. Therefore, we conclude that the measured AFM pull-off forces correspond to adhesive failure.

D. Interfacial adhesion and fracture energies

1. Measured adhesion forces and energies

Adhesion forces between different layers in the Au-coated PDMS structure (Figure 8(a)) are presented in Figure 8(b). The highest adhesion force was obtained between the Cr (adhesion promoter layer) and PDMS. This had an average pull-off/adhesion force of 77 ± 29.3 nN. The high adhesion in Cr/PDMS interface could be due to highly electropositive nature of Cr. It is easy for electrons to be donated from Cr to methyl groups in the side chains of PDMS and form the surface dipoles that increase the attraction. An intermediate adhesion force of 30 ± 5.7 nN was obtained for the Cr-Au interaction, while the lowest adhesion was obtained for the PDMS-Au interaction.

In an effort to use the models described in Sec. II A 2, a non-dimensional parameter for the calculation of the adhesion energy was first found to be $\sim 10^{-6}$ (which is $\ll 0.1$).^{26–28} The DMT model was then used to determine the

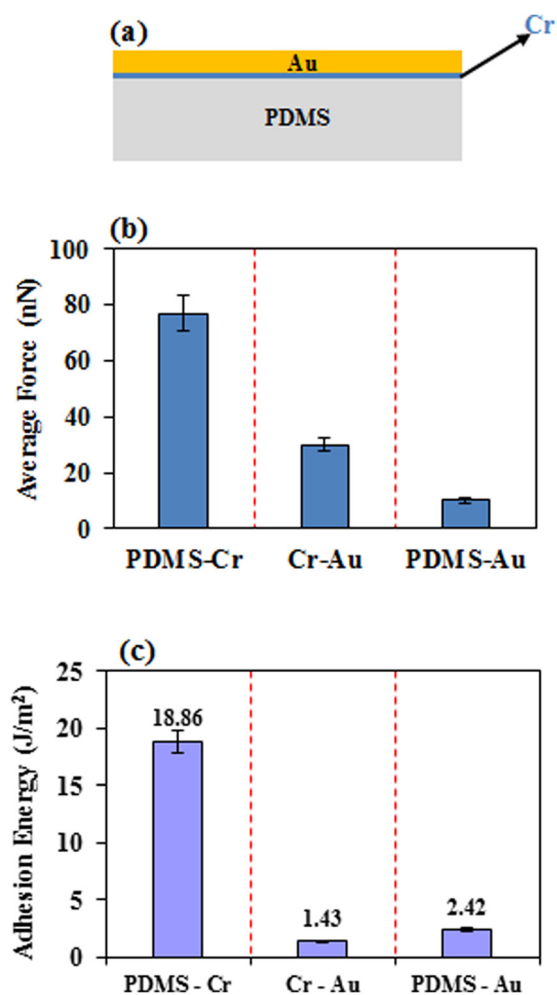


FIG. 8. Interfacial adhesion in Au-coated PDMS structure: (a) schematic of Au-coated PDMS structure with Cr interlayer, (b) average of the measured AFM adhesion forces, and (c) measured AFM adhesion energies.

TABLE III. Interfacial energy release rates obtained from analytical expressions for different pre-strains for cracks between Au films and PDMS substrates.

Pre-strain ε (%)	G_c (J/m ²)	G (J/m ²)	σ_R/σ_c	G/G_c
18.00	2.64	2.71	75.70	1.02
36.00	2.64	2.79	34.60	1.06
70.00	1.92	2.20	12.20	1.14

adhesion energies. The measured rms roughness value of surface 1 and the radius value of the AFM tip (surface 2) were incorporated into Eq. (3) to calculate the effective radius. The measured adhesion forces and the corresponding effective radii were then incorporated into Eq. (2) to calculate the adhesion energies. The results of these calculations are presented in Figure 8(c). Once again, the Cr interlayer exhibits the highest adhesion energy with the PDMS substrate. However, due to the roughness of the Cr layer, the adhesion energies of the Cr-Au couples are now comparable to those between PDMS and Au.

2. Interfacial fracture energies

The calculated interfacial energies obtained for different pre-strain values are summarized in Table III. The ratios of the energy release rates, G , and the critical energy release rates, G_c , obtained from Eqs. (9) and (10), are plotted along with the analytical solutions in Figure 9. The ratios increase to a peak before decreasing to a steady-state value of about 1.0. This is comparable to results from earlier work by Hutchinson and Suo.²⁵

The energy release rates were also computed using ABAQUSTM. Figures 10(a)–10(d) show plots of energy release rate as a function of interfacial crack length. These are presented for buckled Au films of different thicknesses. The interfacial energy release rates decrease continuously with increasing crack length in the case of the 100 nm Au films (Figure 10(a)). However, turning points were observed for thinner 50 and 75 nm Au films (Figures 10(b)–10(d)). In any case, steady state fracture toughness values were approached with increasing interfacial crack length. Also, the turning points corresponded to the onset of buckling, while the differences between the steady state energy release

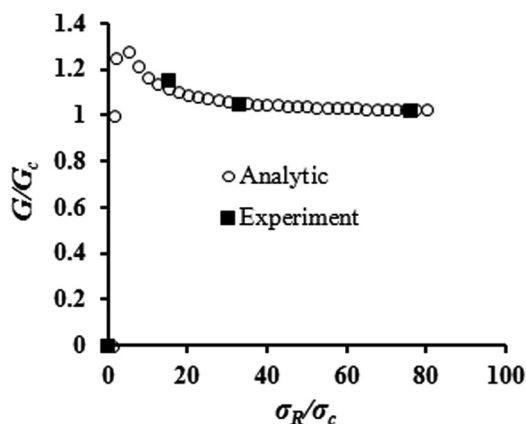


FIG. 9. Plot of G/G_c versus σ_R/σ_c .

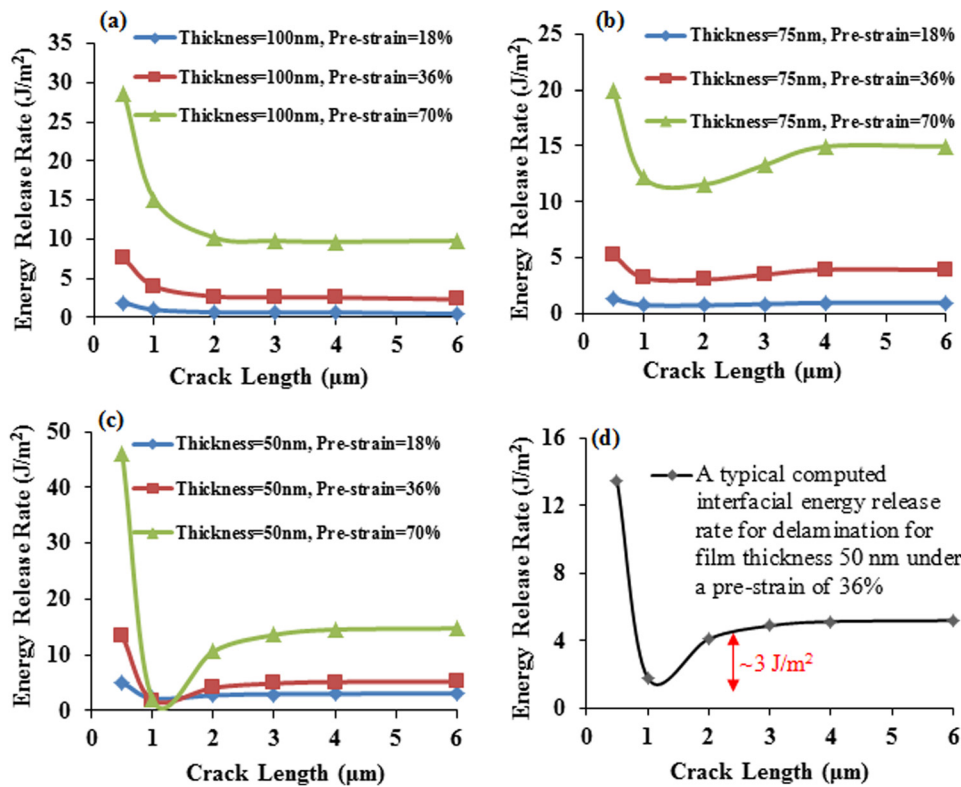


FIG. 10. Interfacial energy release rate (G_{comp}) versus interfacial crack length. (a) 100 nm thick Au films on PDMS substrates; (b) 75 nm thick Au films on PDMS substrates; (c) 50 nm thick films on PDMS substrates; and (d) 50 nm thick film with 36% pre-strain and delamination.

rate and the turning point energy release rate correspond to the interfacial energy for delamination due to buckling.

For example, the computed interfacial energy for delamination of a Au/PDMS structure with a typical thickness (50 nm) of the Au film is $\sim 3 J/m^2$ under pre-strain value of 36% (Figure 10(d)). The von Mises stress distributions in the buckled Au films on PDMS substrates are presented in Figures 11(a)–11(e). The amplitude of the buckled film increases with increasing interfacial crack length. It also suggests that interfacial crack growth can be used to control the waviness of the buckled films prior to applications in stretchable electronics structures.

3. Comparison of adhesion energies and energy release rates

The measured adhesion energies are comparable to the interfacial energy release rates obtained for PDMS-Au interfaces using both computational and analytical techniques. A comparison of the data is presented in Figure 12. Note that the measured adhesion energy of the PDMS-Cr interface was significantly greater than the corresponding calculated interfacial energies. This suggests that the interfaces with the lower interfacial fracture toughnesses dominated the delamination processes that occurred during the buckling of the films on the PDMS substrates.

4. Dependence of interfacial energy on pre-strain and film thickness

For different ratios of interfacial crack lengths to film thicknesses ($2a/h$), the computed interfacial energy release rates are plotted as a function of pre-strain in Figure 13. In obtaining the ratios, the crack length was maintained

constant, while the thickness of the film was varied. The energy release rates increase with increasing pre-strain. However, increasing pre-strain could also result in multiple interfacial cracks, which can cause reduction in the wavelength of the Au-PDMS surface profile. This explains the reduction in the wavelength of the wrinkled Au film

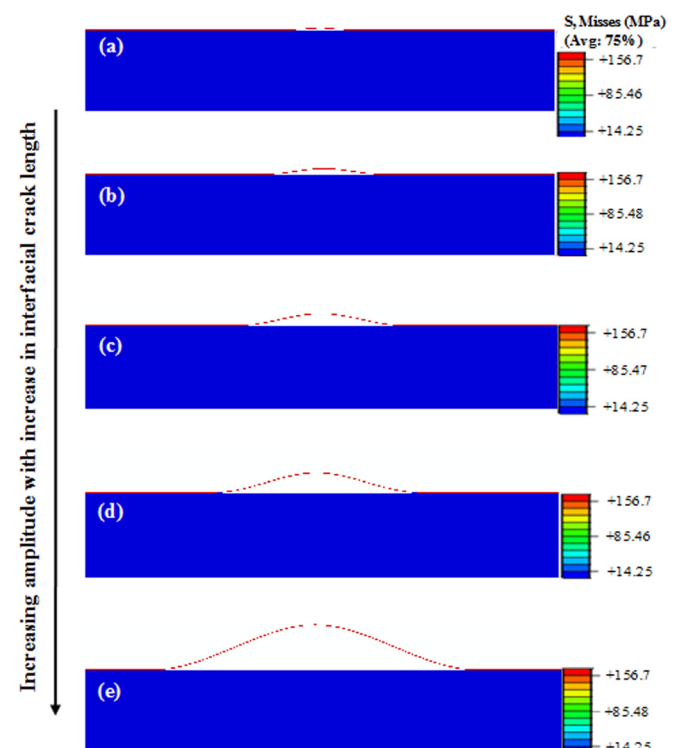


FIG. 11. Von Mises of delamination-induced buckled Au film. (a)–(e) The amplitude increases with increasing interfacial crack length.

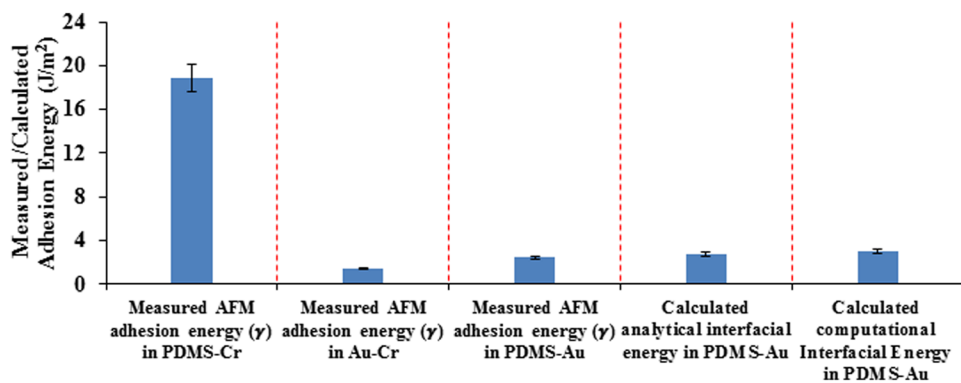


FIG. 12. Comparison of measured AFM adhesion energies and calculated interfacial energy release rates.

observed in Figure 3 for increasing the pre-strain of the PDMS substrate. According to Figure 13, for a thick film ($2a/h = 5$), a small pre-strain ($\sim 20\%$) will cause delamination due to buckling for a critical adhesion energy, $\gamma = 2.42 \text{ J/m}^2$. However, the interfacial energy release rate between a relatively thin film ($2a/h = 90$) and the PDMS substrate is maintained below the critical value at a pre-strain of $\sim 70\%$.

E. Implications

The implications of the above results are quite significant. First, they suggest that a basic understanding of micro-wrinkle and buckle formation is useful in the design and fabrication of micro-scale features in opto-electronic and biomedical structures. In the case of opto-electronic structures, these may include diffraction gratings and electronic textiles, while potential biomedical applications may include implantable biomedical devices for sensing and drug delivery.

The ability to control the surface textures by micro-wrinkling and buckling may also provide biomedical electronic systems with the ability to integrate well with biological tissue. For example, prior work⁵⁷ has shown that micro-grooves with depths and spacings of $\sim 10\text{--}20 \mu\text{m}$ can promote the contact guidance/alignment of biological cells in ways that can lead to reduced scar tissue formation and increased cell/surface integration.⁵⁸ There is, therefore, the potential to tailor future wrinkled and buckled structures that can facilitate cell/surface interactions and integration with biological tissue.

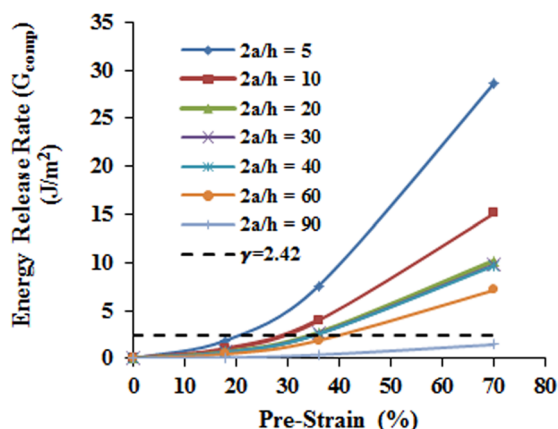


FIG. 13. Interfacial energy release rate (G_{comp}) versus pre-strain.

The interest in the potential stretchable electronics which include solar cells and light emitting devices that require the design of robust systems that are stretchable without significant interfacial failure.⁵ There is, therefore, a need to extend the strain-induced micro-wrinkling and buckling testing technique to a more general framework for the measurement of thin film interfacial fracture toughness. These are clearly some of the challenges and opportunities for future work.

V. SUMMARY AND CONCLUDING REMARKS

This paper presents evidence of micro-wrinkle and delamination-induced buckle formation in thin film structures consisting of nano-scale Au films coated onto the surfaces of stretchable PDMS substrates. The wavelengths of the micro-wrinkled and buckled profiles decrease with increasing pre-strain. The critical buckling stress also decreased with increasing wavelength of the profile. The pre-strain technique was used for the measurement of the interfacial fracture toughness between hard and soft materials. The measurements of interfacial fracture toughness obtained for Au films on PDMS substrates are comparable to AFM measurements of adhesion energy. The results suggest that pre-strain-controlled profiles can be considered for potential biomedical and optoelectronic applications.

ACKNOWLEDGMENTS

The research was supported by the National Science Foundation (DMR 0231418), the Princeton University Grand Challenges Program, the African Development Bank, the World Bank STEP B Program, the World Bank African Centers of Excellence Program and the Nelson Mandela Institution. The authors would also like to thank Professor Barry Royce for useful technical discussions.

¹S. P. Lacour, J. Jones, S. Wagner, T. Li, and Z. Suo, *Proc. IEEE* **93**, 1459 (2005).

²T. Li, Z. G. Suo, S. P. Lacour, and S. Wagner, *J. Mater. Res.* **20**, 3274 (2005).

³D.-H. Kim and J. A. Rogers, *Adv. Mater.* **20**, 4887 (2008).

⁴S. P. Lacour, J. Jones, Z. Suo, and S. Wagner, *IEEE Electron Device Lett.* **25**, 179 (2004).

⁵D.-H. Kim, J. Xiao, J. Song, Y. Huang, and J. A. Rogers, *Adv. Mater.* **22**, 2108 (2010).

⁶C. Yu, K. O'Brien, Y.-H. Zhang, H. Yu, and H. Jiang, *Appl. Phys. Lett.* **96**, 041111 (2010).

- ⁷R.-H. Kim, D.-H. Kim, J. Xiao, B. H. Kim, S.-H. Park, B. Panilaitis, R. Ghaffari, J. Yao, M. Li, Z. Liu, V. Malyarchuk, D. G. Kim, A.-P. Le, R. G. Nuzzo, D. L. Kaplan, F. G. Omenetto, Y. Yang, Z. Kang, and J. A. Rogers, *Nature Materials* **9**, 929 (2010).
- ⁸C. M. Stafford, C. Harrison, K. L. Beers, A. Karim, E. J. Amis, M. R. VanLandingham, H.-C. Kim, W. Volksen, R. D. Miller, and E. E. Simonyi, *Nature Mater.* **3**, 545 (2004).
- ⁹C. M. Stafford, B. D. Vogt, C. Harrison, D. Julthongpipit, and R. Huang, *Macromolecules* **39**, 5095 (2006).
- ¹⁰P. J. Yoo, K. Y. Suh, S. Y. Park, and H. H. Lee, *Adv. Mater.* **14**, 1383 (2002).
- ¹¹M. Watanabe, H. Shirai, and T. Hirai, *J. Appl. Phys.* **92**, 4631 (2002).
- ¹²D. J. Lipomi, B. C. Tee, M. Vosgueritchian, and Z. Bao, *Adv. Mater.* **23**, 1771 (2011).
- ¹³M. Pretzl, A. Schweikart, C. Hanske, A. Chiche, U. Zettl, A. Horn, A. Boker, and A. Fery, *Langmuir* **24**, 12748 (2008).
- ¹⁴F. Wang, M. Xue, and T. Cao, *Adv. Mater.* **21**, 2211 (2009).
- ¹⁵M. T. Lam, W. C. Clem, and S. Takayama, *Biomaterials* **29**, 1705 (2008).
- ¹⁶X. Jiang, S. Takayama, X. Qian, E. Ostuni, H. Wu, N. Bowden, P. LeDuc, D. E. Ingber, and G. M. Whitesides, *Langmuir* **18**, 3273 (2002).
- ¹⁷J. Lee, M. Shi, J. Yoon, S.-I. Park, M. Li, Z. Liu, and Y. Rogers, *Adv. Mater.* **23**, 986 (2011).
- ¹⁸J. W. Hutchinson, *Philos. Trans. R. Soc. London, Ser. A* **371**, 20120422 (2013).
- ¹⁹H. Mei and R. Huang, *Proceedings of the 13th International Conference on Fracture, Beijing, China* (June 16–21, 2013), pp. 1–9.
- ²⁰M. Watanabe, *Soft Matter* **8**, 1563 (2012).
- ²¹Y. Ebata, A. B. Croll, and A. J. Crosby, *Soft Matter* **8**, 9086 (2012).
- ²²Y. Sun, W. M. Choi, H. Jiang, Y. Y. Huang, and J. A. Rogers, *Nat. Nanotechnol.* **1**, 201 (2006).
- ²³W. O. Akande, Y. Cao, N. Yao, and W. Soboyejo, *J. Appl. Phys.* **107**, 043519 (2010).
- ²⁴D. Y. Momodu, T. Tong, M. G. Zebaze Kana, A. V. Chioh, and W. O. Soboyejo, *J. Appl. Phys.* **115**, 084504 (2014).
- ²⁵J. Hutchinson and Z. Suo, *Adv. Appl. Mech.* **29**, 63 (1991).
- ²⁶Y. Mao, W. L. Wang, D. Wei, E. Kaxiras, and J. G. Soderoski, *ACS Nano* **5**, 1395 (2011).
- ²⁷H. Fei, H. Jiang, and D.-Y. Khang, *J. Vac. Sci. Technol. A* **27**, L9 (2009).
- ²⁸H. Jiang, D.-Y. Khang, H. Fei, H. Kim, Y. Huang, J. Xiao, and J. A. Rogers, *J. Mech. Phys. Solids* **56**, 2585 (2008).
- ²⁹D.-Y. Khang, H. Jiang, Y. Huang, and J. A. Rogers, *Science* **311**, 208 (2006).
- ³⁰G. Domokos, P. Holmes, and B. Royce, *J. Nonlinear Sci.* **7**, 281 (1997).
- ³¹P. Holmes, G. Domokos, and G. Hek, *J. Nonlinear Sci.* **10**, 477 (2000).
- ³²J. Yin and X. Chen, *J. Phys. D: Appl. Phys.* **44**, 045401 (2011).
- ³³N. Bowden, S. Brittain, A. G. Evans, J. W. Hutchinson, and G. M. Whitesides, *Nature* **393**, 146 (1998).
- ³⁴N. H. Bowden, T. S. Wilhelm, K. E. Paul, and G. M. Whitesides, *Appl. Phys. Lett.* **75**, 2557 (1999).
- ³⁵Y. Qi, P. K. Purohit, and M. C. McAlpine, *Proc. SPIE* **8031**, 80311R (2011).
- ³⁶Z. Y. Huang, W. Hong, and Z. Suo, *J. Mech. Phys. Solids* **53**, 2101 (2005).
- ³⁷A. Concha, J. W. McIver III, P. Mellado, D. Clarke, O. Tchernyshyov, and R. L. Leheny, *Phys. Rev. E* **75**, 016609 (2007).
- ³⁸J. M. Harris, G. R. Swathilyer, A. K. Bernhardt, J. Y. Huh, S. D. Hudson, J. A. Fagan, and E. K. Hobbie, *ACS Nano* **6**, 881 (2012).
- ³⁹E. K. Hobbie, D. O. Simien, A. Fagan, J. Y. Huh, J. Y. Chung, S. D. Hudson, J. Obrzut, J. F. Douglas, and C. M. Stafford, *J. Phys. Rev. Lett.* **104**, 125505 (2010).
- ⁴⁰Y. Wang, R. Yang, Z. Shi, L. Zhang, D. Shi, E. Wang, and G. Zhang, *ACS Nano* **5**, 3645 (2011).
- ⁴¹M. Ramanathan, S. M. Kilbey II, Q. Ji, J. P. Hill, and K. Ariga, *J. Mater. Chem.* **22**, 10389 (2012).
- ⁴²Y. Wang, P. Kanjanaboos, E. Barry, S. McBride, X.-M. Lin, and H. M. Jaeger, *Nano Lett.* **14**, 826 (2014).
- ⁴³Rev. E. (Digital Instruments, Veeco Metrology, 1999).
- ⁴⁴O. Akogwu, D. Kwabi, A. Munhutu, T. Tong, and W. O. Soboyejo, *J. Appl. Phys.* **108**, 123509 (2010).
- ⁴⁵D. Yu, O. K. Oyewole, D. Kwabi, T. Tong, V. C. Anye, J. Asare, E. Rwenyagila, A. Fashina, O. Akogwu, J. Du, and W. O. Soboyejo, *J. Appl. Phys.* **116**, 074506 (2014).
- ⁴⁶Veeco Instruments Inc., *Improving the Accuracy of AFM Measurements, the Thermal Tune Solution* (Bruker Corporation, Billerica, MA, 2005).
- ⁴⁷B. V. Derjaguin, V. M. Muller, and Y. P. Toporov, *Prog. Surf. Sci.* **45**, 131 (1994).
- ⁴⁸K. L. Johnson, K. Kendall, and A. D. Roberts, *Proc. R. Soc. London, Ser. A* **324**, 301 (1971).
- ⁴⁹D. Maugis, *J. Colloid Interface Sci.* **150**, 243 (1992).
- ⁵⁰N. Rahbar, K. Wolf, A. Orana, R. Fennimore, Z. Zong, J. Meng, G. Papandreou, C. Maryanoff, and W. Soboyejo, *J. Appl. Phys.* **104**, 103533 (2008).
- ⁵¹J. Meng, A. Orana, T. Tan, K. Wolf, N. Rahbar, H. Li, G. Papandreou, C. Maryanoff, and W. Soboyejo, *J. Mater. Res.* **25**, 641 (2010).
- ⁵²S. Youssefian and N. Rahbar, *J. Mech. Behav. Biomed. Mater.* **18**, 1 (2013).
- ⁵³W. W. Gerberich and M. J. Cordill, *Rep. Prog. Phys.* **69**, 2157 (2006).
- ⁵⁴T. Tong, B. Babatope, S. Admassie, J. Meng, O. Akwogu, W. Akande, and W. O. Soboyejo, *J. Appl. Phys.* **106**, 083708 (2009).
- ⁵⁵O. Akogwu, D. Kwabi, S. Midturi, M. Eleruja, B. Babatope, and W. O. Soboyejo, *Mater. Sci. Eng. B* **170**, 32 (2010).
- ⁵⁶I. D. Johnston, D. K. McCluskey, C. K. L. Tan, and M. C. Tracey, *J. Micromech. Microeng.* **24**, 035017 (2014).
- ⁵⁷J. Chen, S. Mwenifumbo, C. Langhammer, J.-P. McGovern, M. Li, A. Beye, and W. O. Soboyejo, *J. Biomed. Mater. Res., Part B* **82B**, 360 (2007).
- ⁵⁸A. Gottschalk and W. R. Schafer, *J. Neurosci. Methods* **154**, 68 (2006).